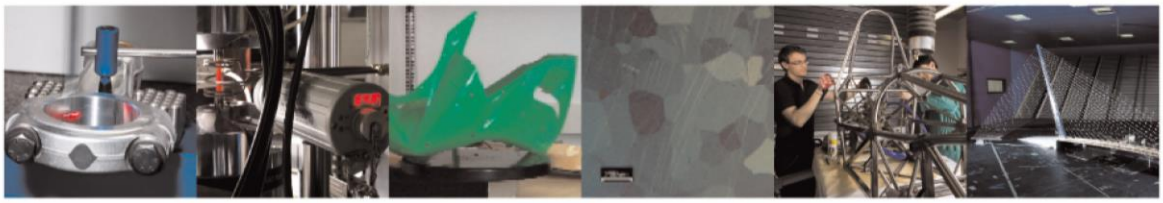

A statistical learning method for image-based monitoring of the plume signature in laser powder bed fusion

Grasso, M.; Colosimo, B. M.

This is a post-peer-review, pre-copyedit version of an article published in ROBOTICS AND COMPUTER-INTEGRATED MANUFACTURING. The final authenticated version is available online at: http://dx.doi.org/10.1016/j.rcim.2018.11.007

DIPARTIMENTO DI MECCANICA ■ POLITECNICO DI MILANO
via G. La Masa, 1 ■ 20156 Milano ■ EMAIL (PEC): pecmecc@cert.polimi.it
http://www.mecc.polimi.it
Rev. 0

A Statistical Learning Method for Image-based Monitoring of the Plume Signature in Laser Powder Bed Fusion

M. Grasso[1] and B. M. Colosimo

Dipartimento di Meccanica, Politecnico di Milano, Via La Masa 1, 20156 Milan (Italy)

marcoluigi.grasso@polimi.it; biancamaria.colosimo@polimi.it

Abstract. *The industrial breakthrough of metal additive manufacturing processes mainly involves highly regulated sectors, e.g., aerospace and healthcare, where both part and process qualification are of paramount importance. Because of this, there is an increasing interest for in-situ monitoring tools able to detect process defects and unstable states since their onset stage during the process itself. In-situ measured quantities can be regarded as "signatures" of the process behaviour and proxies of the final part quality. This study relies on the idea that the by-products of laser powder bed fusion (LPBF) can be used as process signatures to design and implement statistical monitoring methods. In particular, this paper proposes a methodology to monitor the LPBF process via in-situ infrared (IR) video imaging of the plume formed by material evaporation and heating of the surrounding gas. The aspect of the plume naturally changes from one frame to another following the natural dynamics of the process: this yields a multimodal pattern of the plume descriptors that limits the effectiveness of traditional statistical monitoring techniques. To cope with this, a nonparametric control charting scheme is proposed, called K-chart, which allows adapting the alarm threshold to the dynamically varying patterns of the monitored data. A real case study in LPBF of zinc powder is presented to demonstrate the capability of detecting the onset of unstable conditions in the presence of a material that, despite being particularly interesting for biomedical applications, imposes quality challenges in LPBF because of its low melting and boiling points. A comparison analysis is presented to highlight the benefits provided by the proposed approach against competitor methods.*

Keywords: metal additive manufacturing; laser powder bed fusion; in-situ monitoring; infrared imaging; zinc; process plume.

1 Introduction

Laser-based additive manufacturing (AM) of metal parts and laser powder bed fusion (LPBF) systems in particular have been increasingly used in various industrial sectors [1 – 13]. Indeed, LPBF provides a high flexibility for producing parts whose shape complexity, internal structure and material properties can not be achieved with conventional technologies. However, quality-

[1] Corresponding author

related issues play a key role in highly regulated sectors, like aerospace and healthcare, which are currently pulling the industrial breakthrough of AM technologies. As a matter of fact, the process capability, repeatability and stability shall meet the challenging requirements imposed by the industry. Local defects may occur during the laser scanning of one (or more) layers, caused by improper process parameters or supporting strategies, non-homogeneous powder deposition, out-of-control heat exchanges, material contaminations, etc. [2 - 3]. Because of this, many authors and LPBF system developers are devoting continuous research efforts in developing in-line monitoring tools based on in-situ sensing for defect detection and localization. Several quantities that are measurable during the process can be related to the final quality of the part, and hence they can be regarded as *signatures* of the process itself [9]. A large portion of the literature in this framework was devoted to the monitoring of melt pool signatures, i.e. the properties of the powder bed region where the local laser melting occurs [2 – 3; 8 - 9]. This involves the use of sensors (e.g., photodiodes and cameras) placed co-axially to the laser path. Other studies investigated signatures that can be measured with off-axis sensors (e.g., cameras placed outside the laser optical path), including the thermal map, topography and geometry of the printed slice, and the homogeneity of the powder bed [2 – 3; 8 - 9]. More recently, different authors pointed out that also the LPBF by-products, i.e., spatters and plume, can be information drivers for in-situ process monitoring [14 - 22]. A similar conclusion was drawn in few seminal studies in laser welding [23 - 24], which demonstrated that both the spatters and the plume enclose relevant information to determine the stability of the process and the quality of the weld.

Spatters are either powder particles blown away during the laser scan of the part or liquid material ejected from the melt pool as a result of unstable solid-liquid transitions [16 - 17, 20]. The plume, instead, is formed by the partial material vaporization, which may also lead to the formation of plasma as a consequence of metallic vapor ionization [21]. The plume differs from the surrounding atmosphere in terms of chemical composition, temperature and pressure, and it can interfere with the optical properties of the beam path by altering the beam profile and the local energy density [25].

In LPBF, the use of spatters and plume properties as process signatures for the development of in-situ monitoring methodologies was first proposed by Repossini *et al*. [14] and Grasso *et al*. [15]. In particular, [15] was the first study to present an in-situ statistical monitoring tool based on the analysis of the plume properties. This study extends [15] by presenting an automated alarm rule for fast detection of process instabilities based on in-situ monitoring of the process plume in a novel statistical learning framework. Similarly to [15], the proposed approach relies on thermal image streams acquired by means of an off-axis infrared (IR) camera and it involves the estimation of different descriptors that capture the size, orientation and intensity of the plume during the LPBF of each layer. Differently from [15], this study attempts to tackle the continuously time-varying pattern of the plume properties under in-control conditions caused by the natural process dynamics. Indeed, the aspect of the plume changes from one frame to another as the laser scans the part along the predefined trajectory. As an example, Fig. 1 shows three consecutive frames of an IR video acquired during the LPBF process described in Section 2, where the plume passes from a left-oriented hot region (frame 1) to an almost absent one (frame 2) to a right-oriented region (frame 3).

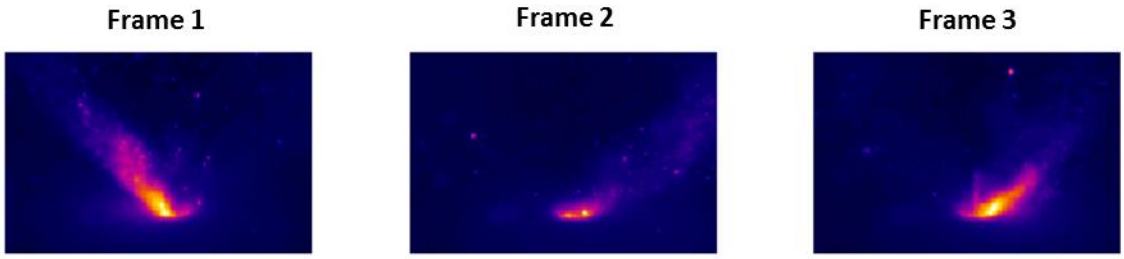

Fig. 1 – Three consecutive frames showing three different states of the plume under in-control process conditions

When traditional control charting schemes are applied to this kind of pattern, poor performances may be achieved. On the one hand, the natural transitions of the plume in the presence of in-control process conditions can inflate the false alarm rates. On the other hand, the underlying dynamics can mask actual out-of-control states and reduce the effectiveness of the

control chart. As a matter of fact, the plume behaviour shown in Fig. 1 yields a clustered pattern of the monitored descriptors, where the transition from one cluster to another is not representative of an out-of-control state unless a real process instability occurs. This corresponds to a so-called "multimode" process, i.e., a process that naturally switches from one in-control state to another [26 - 28]. To deal with this, we propose the use of a nonparametric method, known as K-chart [29 - 35]. It is based on a one-class-classification variant of the Support Vector Machine (SVM) paradigm, called support vector data description (SVDD) [36]. The term "one-class-classification" refers to statistical learning methods that can be trained on a dataset consisting of only natural process data, i.e., data collected under in-control process conditions [37]. The K-chart is applied to the plume descriptors extracted from the in-situ IR video via image segmentation. It is aimed at determining if the process remains stable during the entire production of the part in terms of plume emissions. The SVDD methodology allows one to adapt the alarm threshold to the clustered nature of the monitored descriptors to improve the control chart performances.

The present paper extends [15] by proposing an SVDD-based nonparametric monitoring approach that overcomes the limitations of the previous approach and yields better performances in terms of faster detection of out-of-control states. One further novel contribution with respect to [15] regards the presentation of an improved approach for IR image segmentation, which relies on the same SVM technique used to design the alarm rule. It allows enhancing the identification of the region of interest corresponding to the plume in the IR video frames.

The proposed method was tested in the presence of both stable and unstable LPBF process conditions and compared against benchmark competitors to highlight the provided benefits. In particular, a real case study involving the LPBF of pure zinc is presented. AM processes of zinc and its alloys are highly appealing for customized medical implant manufacturing, but the low melting and boiling points make LPBF of pure zinc and zinc alloys a challenging task. In particular, the low vaporization point of zinc together with its proneness to heat accumulation phenomena, make the plume emission a relevant driver for in-situ process stability monitoring.

Section 2 reviews the state of the art on the analysis of LPBF by-products, with a special focus on in-situ monitoring applications; Section 3 presents the proposed process monitoring methodology; Section 4 describes the real case study dealing with LPBF of zinc; Section 5 presents the achieved results; Section 6 eventually concludes the paper.

2 State of the art

The plume consists of thermally excited high-temperature vapor that originates in correspondence of the melt pool [38]. Some authors also discussed the possible partial ionization into plasma when the evaporated material interacts with the laser radiation [21 - 22]. A large amount of plume can modify the laser beam geometry and the energy input to the material by partially deflecting and absorbing the laser beam energy, or even deviating the laser focus position [24]. Thus, a variation of the characteristics of the plume may be representative of a variation in the energy input conditions and, consequently, of modifications of material properties.

Some authors studied the effect of process parameters on the LPBF by-products by using in-situ sensing methods mainly consisting of very high-speed vision [39 – 40]. The most recent literature [20, 39 – 40] showed that plume emissions are strictly related to spatter ejection phenomena. Indeed, the vapor-driven entrainment of powder particles was shown to be the dominant factor at the origin of spatter ejections in LPBF, whereas liquid metal ejections as a consequence of the recoil pressure in the melt pool play a secondary role on overall by-product emissions [20, 39 – 40]. Ly et al. [20] showed that the hot plume emission generates an induced gas flow inwards the melt pool, which produces a drag force in the vicinity of the melt pool that is sufficient to blow powder particles towards the melt pool. These particles can be consolidated into the track or they pass through the laser path, rapidly heat up and are ejected as incandescent spatters. Bidare et al. [39] showed that the direction of the plume emission determines to a large extent the spatter ejection behavior. By varying the process parameters it is possible to obtain a forward, backward or vertically upward plume emission with respect to the scan direction. Bidare et al. [39] showed that both forward and vertically upward plume emissions may produce a

powder bed denudation caused by the vapor-driven entrainment effect. On the contrary, when a low angle backward plume emission is produced (e.g., at high scanning speed), the plume impinges directly on the powder bed and causes another kind of denudation, where particles are blown away from the track instead of being entrained. This may produce a large amount of cold spatters and just a limited ejection of hot spatters. Ly et al. [20] showed that a backward plume emission can be produced when the recoil pressure is not sufficient to produce a keyhole melting mode, but high enough to form a depression characterized by highest temperature toward the front of the depression. In addition to the plume orientation, Zheng et al. [40] showed that the amount of plume emission and its stability along the track play a relevant role on the amount of spatter ejection and on the quality of the process. The experimental study presented by Zheng et al. [40] showed that in the presence of overmelting conditions at low speed, which caused poor quality track properties, an unstable plume emission was observed. On the other hand, in the presence of lack of fusion regimes at high speed, which caused irregularly shaped tracks, large amounts of plume were observed. The best track quality conditions were met in the presence of intermediate speeds, with small plume emissions and few spatter ejections.

All the aforementioned studies investigated the plume behavior during LPBF of stainless steel, with the only exception of Ly et al. [20] who investigated the LPBF of both stainless steel and Ti6Al4V. Another study, authored by Grasso et al. [15], instead, studied the LPBF of pure zinc. Grasso et al. [15] showed that an instability of the plume size and intensity could be used as a proxy of the process stability and quality. Such evidence was used to design a statistical monitoring method for in-line detection of out-of-control process conditions based on in-situ thermal imaging. A different perspective was investigated by Mumtaz and Hopkinson [41]. Rather than studying a method to monitor the plume behavior, they investigated the possibility of reducing the size of plume and the amount of spatter ejections. In particular they showed that such reduction could be obtained via pulse shaping.

This study extends the research presented by Grasso et al. [15] grounding on the recent enhancements of the general comprehension of physical phenomena that drive the plume

emissions in LPBF, the influence of process parameters and the correlation with the process quality and stability.

3 Proposed methodology

The proposed approach relies on statistical process monitoring of the LPBF plume properties gathered via in-situ thermal imaging. It consists of four major steps shown in Fig. 2, i.e. i) IR image pre-processing, ii) region of interest (ROI) extraction, iii) computation of plume descriptors and iv) *K*-chart design and use. All these steps are described in the next subsections.

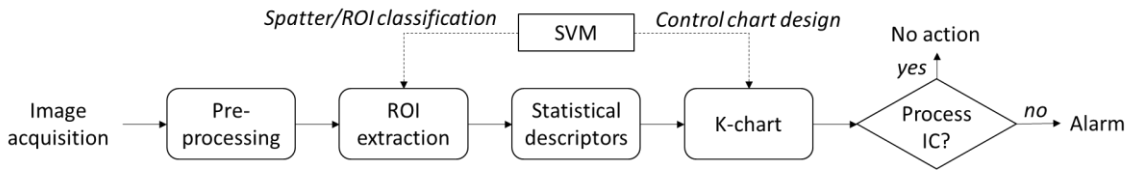

Fig. 2 – Scheme of the proposed approach

3.1 Image pre-processing and ROI extraction

An IR video can be treated as a stream of IR images, $\boldsymbol{U}_j \in \mathbb{R}^{M \times N}$, where $j = 1,2, \ldots$ and $M \times N$ is the size, in pixels, of each frame. Each image is characterized by a dark (cold) background and hot foreground regions that correspond to the laser heated zone (LHZ), the plume and the spatters generated by the laser-material interaction. The plume originates from the LHZ, and hence they can be difficult to separate in video frames. Because of this, we focus the analysis on a ROI that consists of the union of plume and LHZ, although the plume usually represents the largest portion of the ROI.

Fig. 3 shows the sequential operations needed to segment the images and to extract the ROI in each frame.

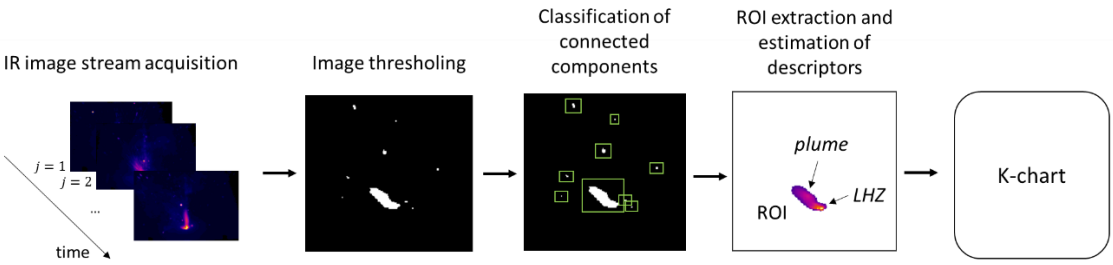

Fig. 3 – Image pre-processing steps required to estimate the ROI's statistical descriptors

The first step is a thresholding operation to binarize the image and identify the connected components corresponding to the ROI and the spatters. A previous study on plume analysis in LPBF [15] showed that the Otsu's algorithm is a computationally efficient and effective technique that yields a reliable segmentation for this application. The second step consists of identifying the connected component that corresponds to the ROI. A few studies for a similar purpose in laser welding [23 - 24; 42] classify the spatters and the plume by setting a limit on the area of the connected components: the smallest ones are classified as spatters and filtered out. An automated method for the selection of this limit was proposed in [15], but a sensitivity analysis showed that wrong choices of the threshold could lead to unsatisfactory monitoring performances. In this study, we propose a different approach, which exploits not only the area of the components but also an information about their location within the frame. Indeed, the ROI is expected to occupy a large area partially overlapped to the region of the slice currently scanned by the laser beam, whereas the spatters are expected to be small components at higher distances from that region. Fig. 4 (left panel) shows the histogram of the areas of all the connected components extracted during the training phase of our case study. Fig. 4 (right panel), instead, shows the scatterplot of the area of all the components against the corresponding distance from the scanned region.

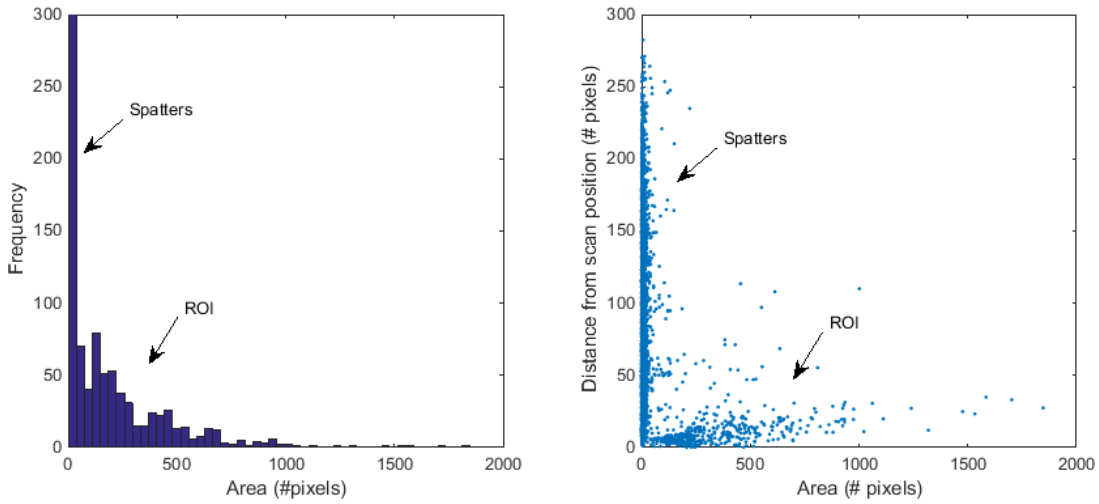

Fig. 4 – Histogram of the areas of all the connected components identified within the training set (left panel) and scatterplot of component area against its distance from the scanned region (right panel)

Fig. 4 shows that the spatters cover a narrow region of the bivariate space corresponding to a wide range of distances and a thin range of areas, whereas the ROIs do the opposite. Contrary to setting a threshold on the area, the proposed approach for ROI classification aims to define a partition of the space spanned by the area and the distance from the scanned region (Fig. 4, right panel). A maximum-margin partition of the bivariate space is proposed, by training an SVM on these data [43]. The SVM is a statistical learning approach whose underlying idea consists of finding the hyperplane with largest distance (margin) from the nearest training data of each class [43]. The maximization of the margin among the classes is aimed at minimizing the generalization error of the classifier.

Let A_i be the area of the i-th connected component and D_i be the Euclidean distance (expressed in pixels) between its centroid and the centroid of the scanned region[2]. Being unknown the label $g_i \in \{spatter, ROI\}$ of the i-th connected component, a two step procedure is needed:

[2] Note that in our application the scanned region is quite small, 5 x 5 mm, and hence its centroid can be used to approximately estimate the distance of the connected component from the currently scanned area. Generally speaking, a more accurate estimate should be based on the instantaneous laser spot location in the powder bed, which implies a synchronization of the IR video acquisition with the laser scan controller.

1. A two-class clustering algorithm (e.g., k-means clustering with $k = 2$) is applied to the bivariate observations $\{A_i, D_i\}$ in the training set, which yields the labels $g_i \in \{spatter, ROI\}$;
2. Then, the bivariate space is partitioned by applying the SVM on the labelled observations $\{A_i, D_i, g_i\}$. In its general formulation, the SVM exploits a kernel function to estimate a flexible separating plane. To this aim, a Gaussian radial basis function (RBF) is proposed for the present application. Being $\boldsymbol{a}, \boldsymbol{b} \in \mathbb{R}^p$, the RBF with kernel width parameter $S \in \mathbb{R}^+$ is defined as follows:

$$K(\boldsymbol{a} \times \boldsymbol{b}) = \exp\left\{-\frac{\|\boldsymbol{a} - \boldsymbol{b}\|^2}{S^2}\right\} \quad (1)$$

The same kernel function is used in the monitoring phase to design the K-chart (see subsection 3.4). The RBF bandwidth parameter, S, can be automatically selected by following the procedure presented in [44].

Once the bivariate space partition has been estimated, the trained SVM classifier is used to label each future connected component as either a spatter or a ROI. A comparison against the method proposed in [15] is discussed in Section 5. It is worth noticing that maximum-margin clustering via SVM has been proposed in the literature to merge the unsupervised and supervised classification steps mentioned above in one single step [45], but the high computational cost makes this solution less attractive for the present application.

3.2 Estimation of plume descriptors

After the image segmentation and ROI classification, a set of statistical descriptors is computed in order to characterize the relevant properties of the ROI signature. When more than one connected component is classified as a ROI in one single frame, the final ROI is generated as the union of all those components. As an example, this may happen in the presence of bimodal plumes or ROIs where the plume and the LHZ are observed in two distinct connected components. Fig. 5 shows the ROIs extracted from the same frames shown in Fig. 1. The boundary of the ROI

is shown in red. The ellipse that fits the ROI is shown in green: it is the ellipse having the same normalized second central moments, $\mu_{20}, \mu_{02}, \mu_{11}$, as the ROI, where:

$$\mu_{pq} = \frac{\sum_{x=1}^{M_{ROI}} \sum_{y=1}^{N_{ROI}} (x - \mu_x)^p \left(y - \mu_y\right)^q I(x,y)}{\sum_{x=1}^{M_{ROI}} \sum_{y=1}^{N_{ROI}} I(x,y)} \tag{2}$$

$I(x,y)$ is the temperature intensity of the ROI's pixel at x and y coordinates, whereas M_{ROI} and N_{ROI} are the number of pixels along x and y that belong to the ROI. The orientation of the fitted ellipse with respect to the horizontal axis is called ϑ and is such that $\vartheta \in [-90°, 90°]$.

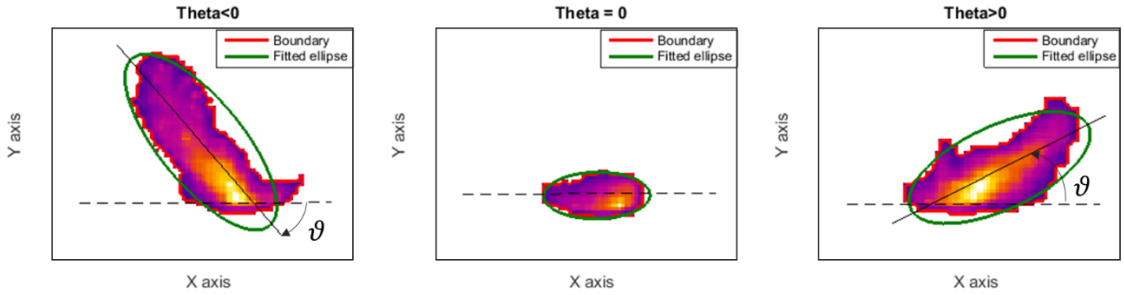

Fig. 5 – Examples of ROIs extracted from the frames shown in Fig. 1

Three statistical descriptors were selected to characterize the signature of the ROI: the area, $A_{ROI,j}$, expressed as the overall number of pixels of the ROI; the average temperature intensity, $I_{ROI,j}$, normalized with respect to the camera temperature range such that $I_{ROI,j} \in [0,1]$, and the absolute orientation, $\vartheta_{ROI,j} = |\vartheta_j| \in [0,90°]$, $j = 1,2,\ldots$. Different authors [23 - 24] pointed out that the size of the plume is a relevant descriptor for in-process quality characterization in laser welding. Indeed, the larger is the plume the higher is the potential deflection and absorption of the laser beam energy. Moreover, the size of the plume can be a proxy of heat accumulation in the part, which is relevant to detect unstable conditions related to bubble formation and pressure increase around the laser-material interaction zone [46].

The average temperature intensity can be a proxy of the amount of material vaporization and heating of the surrounding gas. The temperature is affected by the plume chemical composition and the possible occurrence of ionization. Thus, it potentially provides complementary information with respect to the plume area descriptor. Eventually, the orientation of the plume is relevant because, being equal the plume area, a horizontal orientation of the plume (e.g. ϑ_{ROI} close to 0°) is expected to affect to a lower extent the laser beam absorption and deflection with respect to a vertical orientation (e.g. ϑ_{ROI} close to 90°). Moreover, [24] showed that the polar coordinates of the plume centroid, representative of its orientation, have a close relationship with the actual welding quality. Moreover, recent studies in LPBF [39 – 40] discussed in Section 2 showed that the orientation of the plume is a relevant descriptor of the process stability and the solidified track quality. In this study, only forward oriented plume emissions were observed in different process conditions, and the transition from left to right oriented plumes in in-situ images was only caused by the scan direction of the laser when the frame was acquired. Because of this, the absolute plume orientation was considered in this study, as left-oriented and right-oriented plumes with equal ϑ_{ROI} are expected to be representative of specular conditions and to have an analogous interference with the laser beam.

3.3 Nonparametric process monitoring via K-chart

The proposed approach relies on the assumption that the plume properties should remain stable over time during the entire process under IC conditions. Therefore, we propose using a small set of initial layers as training dataset to design the control chart that will be used to monitor any following layer. This approach is suitable for the specific case of LPBF on pure zinc, where a possible out-of-control condition consists of a heat accumulation that may lead to a drastic failure of the process. Generally speaking, the same control charting scheme can be extended to series production where the training dataset may be collected during the production of copies of the same part.

In order to highlight the need for a nonparametric method, Fig. 6 shows the scatterplots of the three statistical descriptors computed for all the frames acquired under in-control conditions during the LPBF of pure zinc in the experimental case study that is described in Section 4.

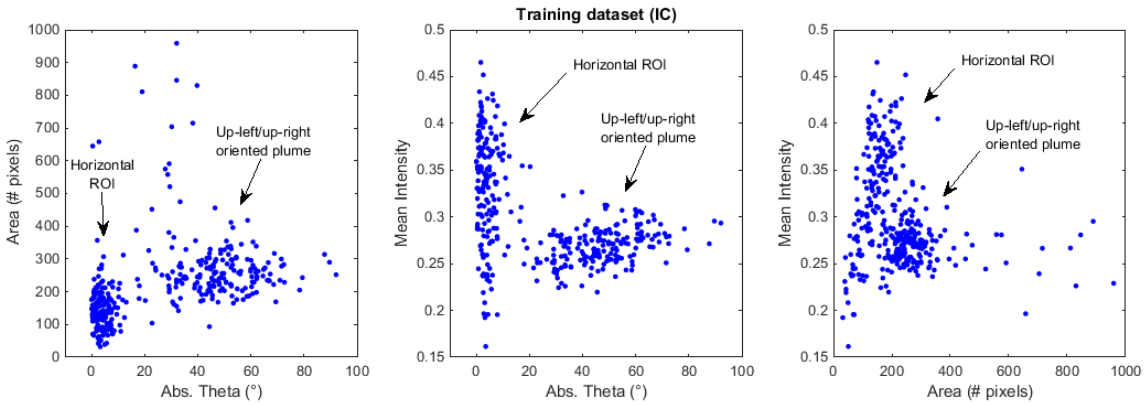

Fig. 6 – Scatterplots of the statistical descriptors belonging to the training dataset of the IC Scenario described in Section 4

Fig. 6 shows two major clusters, one corresponding to the frames where the ROI mainly consists of the LHZ (orientation close to zero, small area and a wide variability in terms of mean intensity[3]), and one corresponding to the frames where the ROI mainly consists of the plume (larger areas, orientations larger than about 20° and a smaller variability in terms of mean intensity). Any transition between one cluster and the other should not be signalled as an alarm because such a transition is the consequence of the natural process dynamics. Such clustered pattern of monitored variables is representative of so-called multimode processes. Various authors studied control charting schemes for this kind of process data. They can be mainly divided into two categories [26, 28], namely the *global modelling* approach [47 – 48] and the *multi-modelling* approach [49 – 50]. Both the methods assume the availability of a training dataset that characterizes the natural process behaviour in different operating modes. The global modelling approach consists of designing a single control chart that is globally able to monitor the process

[3] Due to the fact that the LHZ may be captured during different stages of its cooling transitory, from high intensities to lower ones.

in every known state. The multi-modelling approach, instead, consists of designing one control chart for each distinct in-control mode, such that only the information related to the in-control state that matches the current observations is used for monitoring purposes. This second approach is applicable when different modes are well separable from each other via a preliminary classification step. In our application, plume descriptors in different clusters can be partially or largely overlapped, which makes the multi-modelling approach poorly effective, as initial misclassification errors may strongly affect the control chart performances. To avoid this, we advocate the global modelling framework. In particular, we propose the one-class-classification SVM methodology that allows estimating a control region that adapts to the natural multivariate spread of the descriptors shown in Fig. 6. The K-chart methodology exploits that region to determine if any new multivariate observation is in-control or not. The control statistic consists of the kernel distance of any observation from the multivariate center of the aforementioned control region. Contrary to the traditional T^2-based elliptical region, the shape flexibility of the control region is achieved thanks to one additional degree of freedom provided by a kernel function. The methodology is an extension of the SVM approach, and it is briefly described hereafter. Given the 3-variate training dataset $\{\boldsymbol{x}_j = [A_{ROI,j}, I_{ROI,j}, \vartheta_{ROI,j}]^T, j = 1, \dots, K\}$, the SVDD works by estimating a minimal volume region centered in $\boldsymbol{o} \in \mathbb{R}^3$ and with radius R by solving the following optimization problem:

$$\begin{aligned} &\min\ (R^2 + C \sum_{j=1}^{K} \xi_j) \\ &\text{s.t. } (\boldsymbol{x}_j - \boldsymbol{o})^T (\boldsymbol{x}_j - \boldsymbol{o}) \leq\ R^2 + \xi_j \text{ and } \xi_j \geq 0, j = 1, \dots, K \end{aligned} \tag{3}$$

where $\xi_j, j = 1, \dots, K$, are slack variables, and C is a penalty coefficient used to weight the trade-off between the volume of the region and the percentage of enclosed data ($C > 0$). By introducing the Lagrangian function:

$$L(R, \boldsymbol{o}, \xi_j; \alpha_j, \gamma_j)$$
$$= R^2 + C\sum_{j=1}^{K}\xi_j - \sum_{j=1}^{K}\alpha_j(R^2 + \xi_j - (\boldsymbol{x}_j - \boldsymbol{o})^T(\boldsymbol{x}_j - \boldsymbol{o})) \quad (4)$$
$$- \sum_{j=1}^{K}\gamma_j\xi_j$$

and by setting the partial derivatives w.r.t. R, $\boldsymbol{o}$, and ξ_j, $j = 1, \dots, K$, to zero, problem (1) can be simplified as follows [34]:

$$\begin{aligned} &\max \left(\sum_{j=1}^{K}\alpha_j \boldsymbol{x}_j{}^T\boldsymbol{x}_j - \sum_{j,k=1}^{K}\alpha_j\alpha_k \boldsymbol{x}_j{}^T\boldsymbol{x}_k\right) \\ &\text{s.t. } \sum_{j=1}^{K}\alpha_j = 1 \text{ and } 0 \le \alpha_j \le C, j = 1, \dots, K \end{aligned} \quad (5)$$

Analogously to the margin in the traditional SVM problem [43], the shape of the region is determined by support vectors only, i.e., by the points whose Lagrangian coefficients are larger than zero [34]. Eventually, the control statistic (kernel distance $kd(\boldsymbol{z})$ of any new observation $\boldsymbol{z} \in \mathbb{R}^3$ from the center $\boldsymbol{o}$**)** is estimated by replacing the inner product $\boldsymbol{a}^T\boldsymbol{b}$ with a kernel function $K(\boldsymbol{a} \times \boldsymbol{b})$:

$$kd(\boldsymbol{z}) = K(\boldsymbol{z} \times \boldsymbol{z}) - 2\sum_{j=1}^{K}\alpha_j K(\boldsymbol{x}_j \times \boldsymbol{z}) + \sum_{j,k=1}^{K}\alpha_j\alpha_k K(\boldsymbol{x}_j \times \boldsymbol{x}_k) \quad (6)$$

The RBF kernel function is the common choice for the K-chart implementation and one previous study [35] showed that it is suitable to deal with clustered data. Because of this, the RBF function is used in this study. An automated method for the selection of the kernel parameter, S, was proposed by Tax and Duin [36] and tuned by Ning and Tsung [34]. It extends the kernel selection methodologies used in multi-class SVM problems to the one-class-classification framework. This kernel selection method was used in this study.

By comparing different design solutions, Ning and Tsung [34] showed that the highest control chart performances are achieved by setting $C > 1$. In this case, the constraint $0 \le \alpha_j \le C$ is replaced by $\alpha_j \ge 0$, and problem (5) can be solved by introducing the kernel function $K(\boldsymbol{x}_\cdot \times \boldsymbol{x}_\cdot)$

without penalty. Thus, the kernel radius of the control region can be controlled only by setting the control limit corresponding to the $100(1-\alpha)\%$ empirical percentile of the kernel distance $kd(\boldsymbol{z}_j)$, $j = 1, \dots, K$ [34], where α is the targeted Type I error. This is the control limit used to determine if any observation is in-control or not.

4 Real case study

The real case study consists of the production of zinc specimens via LPBF. Zinc and its alloys are biodegradable metals, i.e., materials that provide a dissolution of the medical device (e.g., cardiovascular stents) inside the human body once it has fulfilled its duty [51]. However, the LPBF of pure zinc is particularly challenging because of its very low melting ($T_m = 693\ K$) and vaporization ($T_v = 1180\ K$) points that are responsible for a large plume formation [52]. Previous studies in laser welding showed that the process plume formation is inflated by the fact that zinc is highly prone to vaporization under laser irradiance [45]. Another challenge related to the LPBF of pure zinc is related to the heat accumulation that may lead to a partial disintegration of the part at high energy density levels [15]. The defect does not manifest immediately, but occurs after a certain number of layers. It can not be completely avoided by selecting an adequate choice of process parameters, because heat accumulation also depends on the local shape of the scanned part. In the presence of temperature sensitive materials like zinc, an increase of heat accumulation in the part may lead to a larger process plume formation. All these issues motivate the investigation of the plume properties as relevant in-situ measurable quantities for the design of LPBF monitoring methods in the presence of critical materials like pure zinc.

In this study, we tested the LPBF process on a prototype system equipped with a fiber laser source with 1 kW maximum power (IPG Photonics YLR-1000) coupled to a scanner (El.En. Scan Fiber) (see [15] for additional details about the experimental setup). Cubic specimens of size $5 \times 5 \times 5\ mm$ were produced with a layer thickness of 50 μm in the presence of different conditions. In the first scenario (denoted by IC), three sets of process parameters were tested, which led to an in-control (IC) process and dense parts (density in the range 96.2 - 98.7%

measured with the Archimede's method). In the second scenario, two different sets of parameters that led to out-of-control (OOC) process states and final part disintegration were tested (denoted by OOC1 and OOC2, respectively). The different sets of process parameters are summarized in Table 1. In particular, three parameters were varied: the laser power, P, the scan speed, v, and the hatch distance, h_d, i.e., the distance between adjacent scan tracks. The scan direction was kept fixed in each layer, corresponding to a pathway from left to right. A future development involves the test of the proposed approach to more general scan strategies.

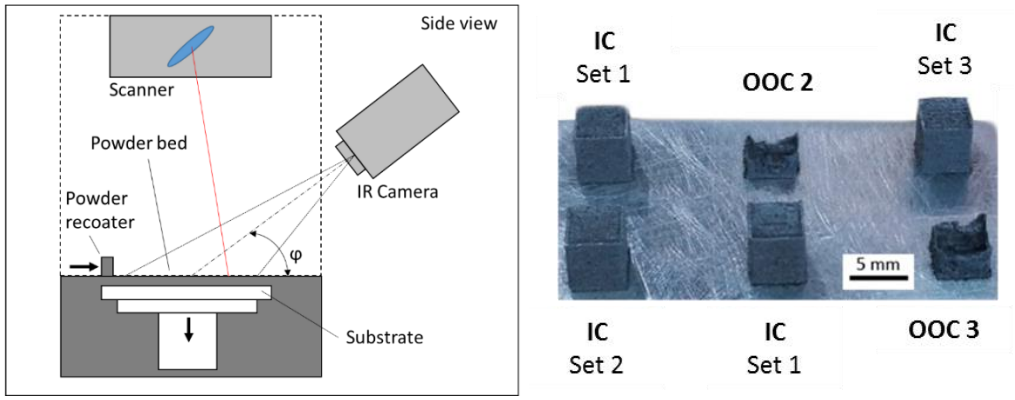

Fig. 7 – Left panel: IR camera setup; right panel: specimens produced under in-control (IC) and out-of-control (OOC1 and OOC2) process conditions

Table 1 – LPBF process parameters used in different scenarios

Scenario		Laser power, P (W)	Scan speed, v (mm/s)	Hatch distance, h_d (μm)
IC	Parameter set 1	110	475	160
	Parameter set 2	195	679	160
	Parameter set 3	195	475	160
OOC 1		195	475	78
OOC 2		195	270	160

A FLIR SC3000 (spectral range of 8 – 9 μm, sampling frequency $f_s = 50\,Hz$, 320×240 pixels) was mounted as shown in Fig. 7 (left panel). It is worth noting that a sampling frequency of $f_s = 50\,Hz$ is representative of the current state-of-the-art on in-situ thermography in LPBF [2 – 3; 8 - 9], but also of some near IR sensing configurations available in commercial systems [2]. However, it necessarily implies a sub-sampling of the plume formation dynamics. Although this

reduces the capability of detecting quick transient phenomena, the preliminary study discussed in [15] showed that it is sufficient to capture major out-of-control patterns related to the plume behaviour. In particular, it was shown in [15] that out-of-control plume patterns were visible in different consecutive frames acquired at $f_s = 50\,Hz$, which allows using such sampling frequency as a compromise choice between the capability of properly characterizing the aspect of the plume, and the computational cost for in-situ image processing and analysis.

The IR camera was calibrated considering only the emissivity of the material in its solid state[4], which is deemed sufficient to analyse relative variations of the temperature either in space or time, although it does not provide reliable absolute temperature measurements.

During the LPBF process of all the specimens, 14 non-consecutive layers were monitored. The first four monitored layers were used as training dataset. Generally speaking, the choice of the number of layers to be used in the training phase should result from a compromise between the reactivity of the monitoring tool and the need to collect a sufficient amount of data to reliably start monitoring the process. The next ten monitored layers were spaced five layers apart, and they were used to test the performances of the proposed method. The collapse of cubes in Scenario OOC1 and OOC2 started to be evident in the last layers, especially in Scenario OOC2, where the plume emissions considerably increased, eventually leading to some sort of explosion (see Section 5). However, the aim of the proposed methodology consists of anticipating the detection of the process instability by signalling an alarm since its onset stage.

5 Discussion of results

The results achieved in the real case study of LPBF on zinc powder are presented hereafter. Subsection 5.1 describes the results related to the image pre-processing step, with a comparison against the alternative method proposed in [15]. Subsection 5.2 presents the monitoring results

[4] An accurate calibration in LPBF is known to be complicated or even impossible because the material undergoes phase changes during the process. However, a temperature intensity indicator is deemed sufficient for relative comparison and stability monitoring purposes.

achieved by applying the proposed monitoring methodology. Subsection 5.3 presents a comparison study against alternative process monitoring approaches.

5.1 ROI classification performances

Fig. 8 shows an example of the maximum-margin partition for ROI classification achieved by using the proposed approach based on the SVM methodology (left panel), compared against the partition corresponding to the threshold on the area descriptor (right panel) described in [15].

Fig. 8 (right panel) shows that some large spatters at high distances from the currently scanned region were classified as ROIs when the competitor method proposed in [15] was applied. Three examples of these spatters are shown in Fig. 9.

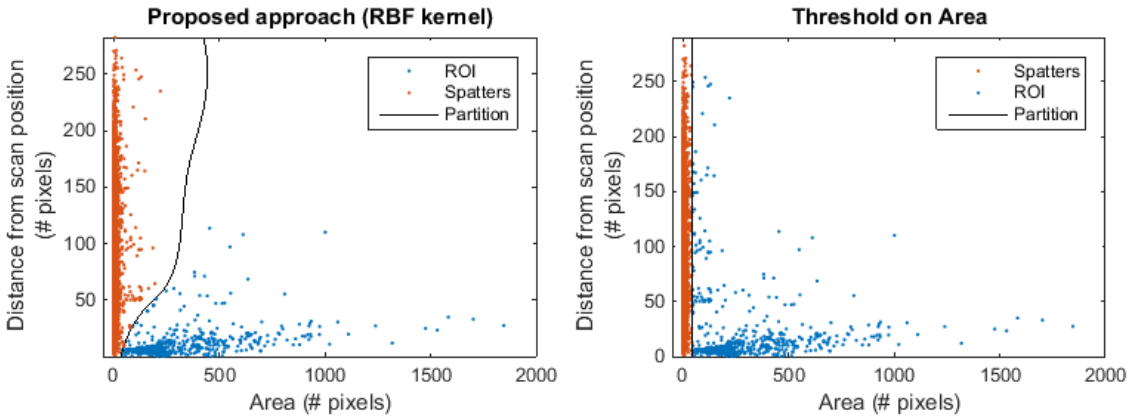

Fig. 8 – Classification between spatters an ROIs based on our propose approach (left panel) and area thresholding [15] (right panel)

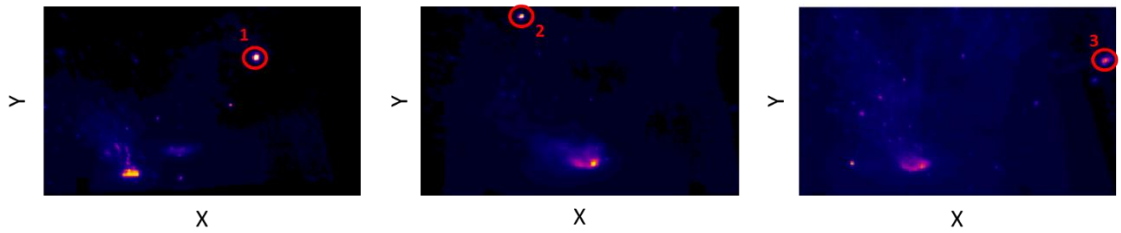

Fig. 9 – Example of spatters misclassified by the approach based on area thresholding

Table 2 compares the effectiveness of the proposed classification method against the competitor one in terms of overall confusion matrices. The confusion matrix was determined by inspecting all the frames belonging to the dataset. Table 2 shows that by setting a threshold on the area descriptor, 4% of larger spatters are misclassified as ROIs, whereas the proposed approach reduces this error to 0.8% thanks to a better partition of the bivariate space. The SVM-based partition enhances the classification of large spatters that are far away from the current melting area without loosing classification capability for small spatters close to the scanned area. A wrong inclusion of large spatters into the ROI inflates the variability estimation for the monitored plume descriptors. The K-chart performances coupled with both the classification methods shown in Fig. 8 are compared in the next sub-section.

Table 2 – Confusion matrices for the proposed classification approach and the one based on the area threshold [15]

Proposed approach (SVM)			Area threshold		
Actual class	Result of classification		Actual class	Result of classification	
	ROI	Spatter		ROI	Spatter
ROI	**99.7%**	0.3%	ROI	99.1%	0.9%
Spatter	0.8%	**99.2%**	Spatter	4.0%	96.0%

5.2 K-chart performances

The scatterplots of the ROI descriptors belonging to the training set of IC Scenario were shown in Fig. 6, where the presence of two major clusters was highlighted. The scatterplots of the same descriptors belonging to the training sets of Scenario OOC1 and Scenario OOC2 are shown in Fig. 10 and Fig. 11, respectively. In OOC scenarios the area of the ROI reaches considerably higher values than the ones observed under IC conditions. In addition, the separation between the two clusters is less evident or even absent. The K-charts for both IC and OOC scenarios are shown in Fig. 12, where the vertical dashed line separates the training phase from the actual monitoring phase. The monitored layers are numbered from 1 to 14. A comparison between plume descriptors acquired during the training phase and the ones signalled by the K-chart as out-of-control in Scenario OOC1 and OOC2 is shown in Fig. 13.

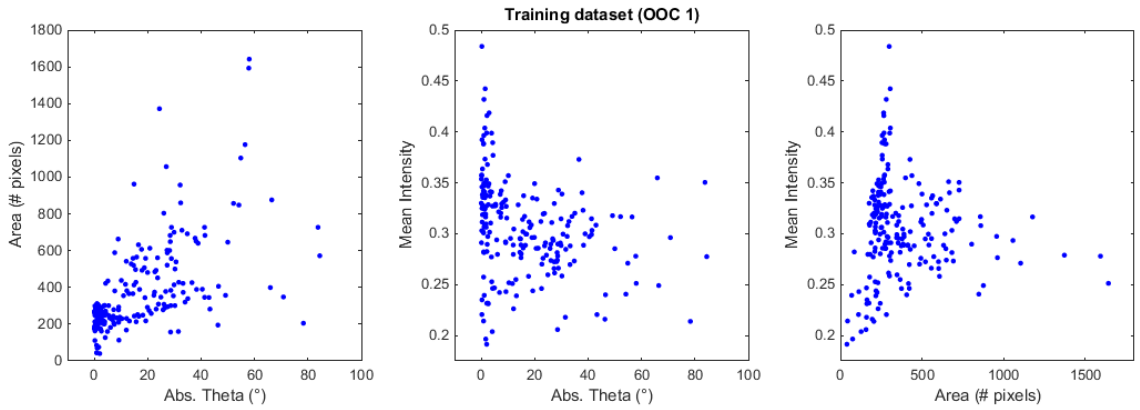

Fig. 10 – Scatterplots of the statistical descriptors in Scenario OOC 1, training set

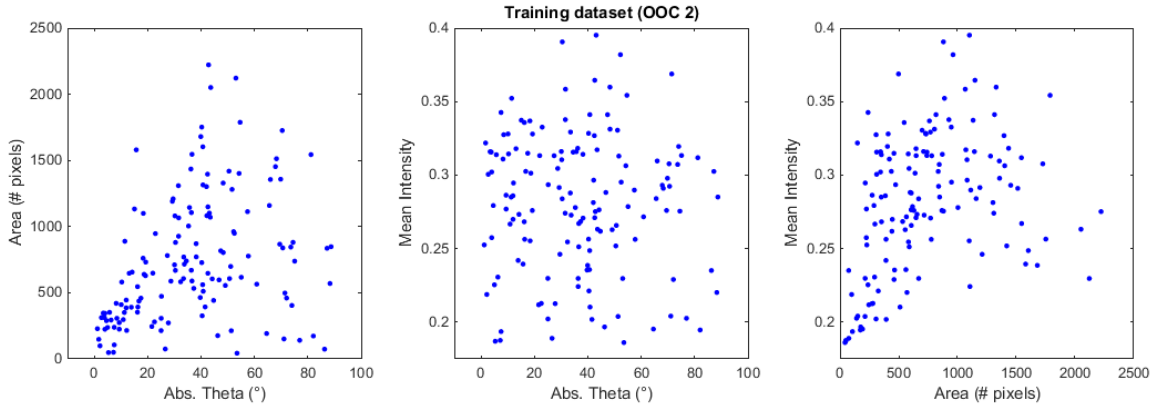

Fig. 11 – Scatterplots of the statistical descriptors in Scenario OOC 2, training set

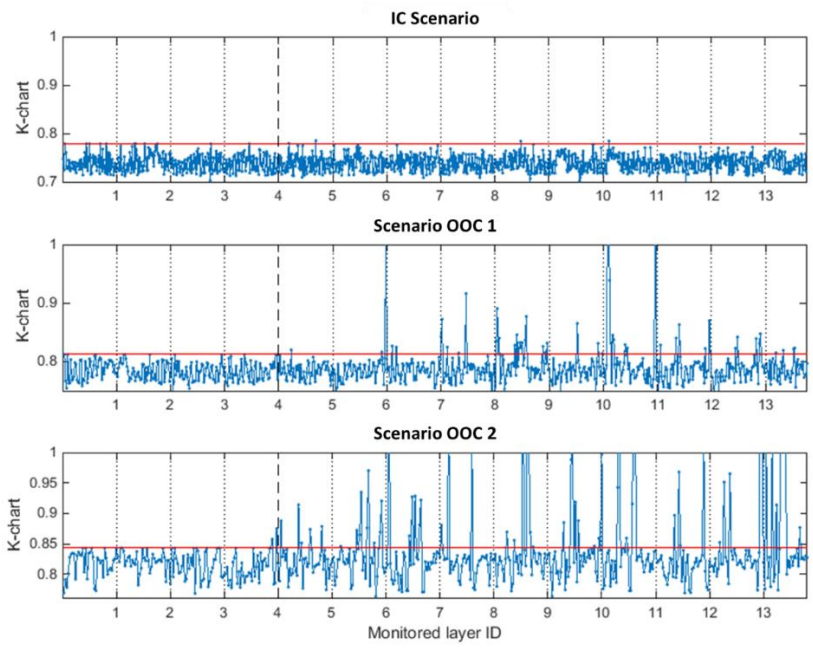

Fig. 12 – K-charts in Scenario IC, OOC 1 and OOC 2; vertical dotted lines separate the monitored layers; the vertical dashed line separate the training from the monitoring phase

Fig. 12 (top panel) shows that in the IC Scenario the process was stable. The three sets of process parameters that generated dense parts also yielded a stable scattered distribution of the ROI statistical descriptors. Fig. 12 (central panel) shows that, in Scenario OOC1, the control chart signalled several out-of-control values that are far beyond the control limit. Fig. 13 shows that the most severe out-of-control observations are mainly caused by ROIs whose area is larger than the areas observed during the training phase. This size increase occurred both at low and high angles ϑ without any evident temperature intensity increase. This can be interpreted in terms of a process instability that produced material vaporization bursts consisting of plume emissions that were larger in size but not at higher temperatures than the ones observed in the first layers. The continuous occurrence of those bursts eventually led to part disintegration.

Fig. 12 (bottom panel) shows that the chart signalled an even larger amount of out-of-control observations in Scenario OOC2, starting soon after the end of the training phase. Fig. 13 shows that, also in this case, there is a considerable increase of the area at different orientation angles without any significant intensity increase with respect to the training phase, although the largest deviations in Scenario OOC2 were observed in correspondence of higher average intensities than in Scenario OOC1. Indeed, during the last monitored layers in Scenario OOC2, a sort of explosion was observed, with a very large ROI that moved towards the upper part of the frame as shown in Fig. 14. This event corresponds to the large consecutive OOC peaks of the kernel distance statistic in Fig. 12 (bottom panel). Although this is an evident symptom of an OOC process, it is the last effect of an unstable melting condition that started in the previous layers. Considering that the monitored layers were spaced five layers apart, the unstable condition in Scenario OOC2 could be detected at least 45 layers before the event shown in Fig. 14. This suggests that the plume is a suitable source of information to characterize the signature of the process and to determine its stability over time. Moreover, the K-chart based on the proposed statistical descriptors is able to detect the instability of the LPBF process at an early stage, by exploiting a training phase at the beginning of the current process itself.

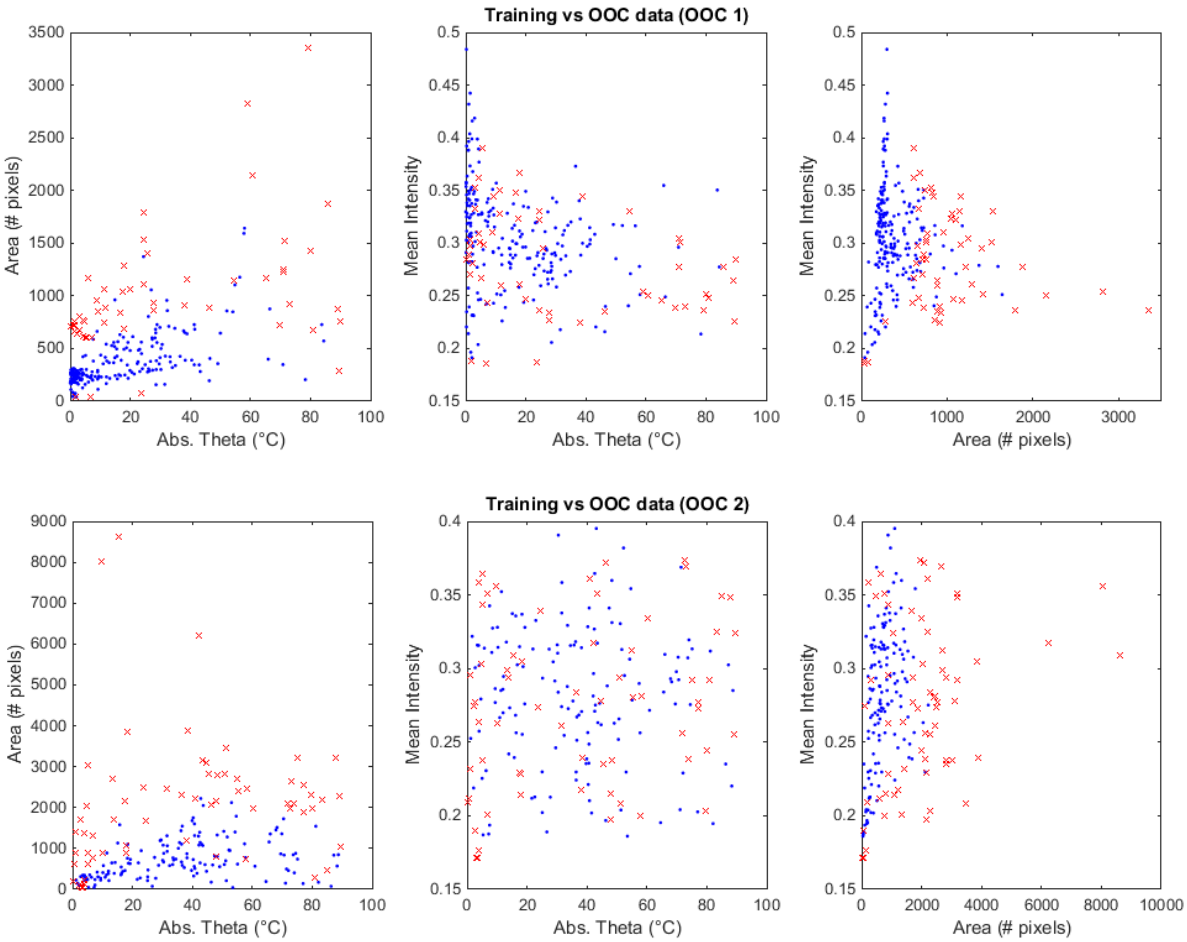

Fig. 13 – Comparison between ROI's descriptor values in the training set (blue points) and the ones signalled by the K-chart (red crosses) in Scenario OOC1 (top panels) and OOC2 (bottom panels)

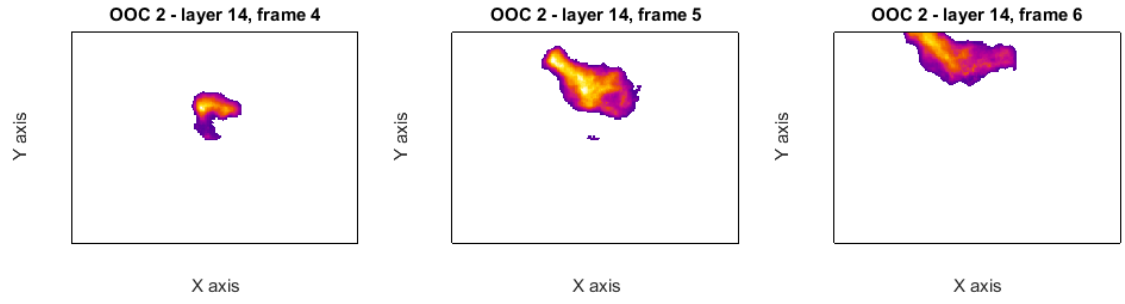

Fig. 14 – Example of ROIs extracted in three consecutive out-of-control frames in Scenario OOC 2

4.3 Comparison against competing methods

The proposed approach was compared against four alternative methods. The first competitor consists of the same K-chart monitoring scheme proposed in this study, but it relies on applying

a threshold on the area of the connected components to classify ROIs and spatters as proposed in [15], instead of using the SVM-based approach. This allowed us to determine the impact of the ROI classification effectiveness on the final control chart performances. The second competitor is the control charting scheme previously proposed in [15], where a Hotelling's T^2 control chart on plume descriptors was used. This type of chart relies on the assumption that the monitored descriptors are drawn from a multivariate normal distribution, but we showed that this assumption is not applicable in the presence of a multimode pattern like the one that characterizes the plume behaviour. Two additional competitor methods were included as they are representative of simple control charting schemes that could be easily implemented by practitioners in the present case study. The third competitor consists of applying multiple univariate control charts to individual plume descriptors, by using the Bonferroni's correction to control the familywise Type I error [53]. This can be seen as a possible extension of previous studies in laser welding [23 - 24], where plume descriptors were individually analyzed. The last competitor is representative of the easiest image-based monitoring scheme that could be implemented by practitioners. It consists of applying a univariate control chart to the average pixel intensities of IR video frames. In this case, no image pre-processing was needed. The control limits of both univariate control charts and Hotelling's T^2 control charts were based on a kernel density estimator [54] to estimate the empirical percentiles of the in-control distribution of the monitored statistics. In order to perform a fair comparison, the control limits of all the compared methods were set in such a way that the false alarms observed in the IC Scenarios were equal to the target Type I error. The synthetic metrics used to compare the methods were: i) the number of the monitored layer where a first alarm was signalled (e.g., "1" means that the first alarm was signalled during the first layer after the training phase), ii) the average run length (ARL) computed as $ARL = 1/(1-\beta)$ where β is the Type II error (i.e., the false negative rate). The ARL indicates the average number of frames before an OOC state is detected. The lower is the ARL, the faster is the control chart in detecting the unstable process condition.

Table 3 – Comparison of competing methods performances in terms of delay to first signal and ARL in OOC scenarios

Method		First signal at layer		ARL	
		OOC 1	OOC 2	OOC 1	OOC 2
Proposed approach		**1**	**1**	**9,77**	**5,76**
Competitor 1	K-chart with area-based plume-spatter classification	**1**	**1**	14,04	7,03
Competitor 2	T^2 chart on plume descriptors	2	2	45,04	120,48
Competitor 3	Univariate charts on plume descriptors	6	4	49,75	151,52
Competitor 4	Univariate chart on overall image intensity	10	11	161,29	136,99

Table 3 shows that the K-chart methodology coupled with the SVM-based classification of the ROI (proposed approach) is the faster method to detect the unstable process conditions. It signalled the OOC states in the first layer after the training phase, with an average number of frames before the signal lower than 10. The same control chart coupled with the area threshold-based classification (competitor 1) yields a slightly higher ARL, but is it able to detect the OOC state in the first layer as well. The slightly lower detection capability of Competitor 1 is caused by the fact that the larger misclassification error between ROIs and spatters inflates the variability of the control statistic, which also inflates the control limit and reduces the effectiveness of the K-chart in the presence of an unstable process.

Competitor 2, based on the Hotelling's T^2 control chart on plume descriptors [15] yielded a lower detection capability. This is caused by the fact that the T^2 control chart applies a control region that corresponds to an ellipsoid in the three-variate space spanned by the plume descriptors. However, as shown above, the actual scatter of the descriptors is far from approaching a multivariate normal one. Therefore, competitor 2 results effective only in the presence of very severe deviations from the training pattern. This reduces the capability of detecting an unstable state of the process since its onset stage.

The Hotelling's T^2 control chart on plume descriptors and the multiple univariate control charts on the same descriptors, i.e., competitors 2 and 3, were characterized by similar

performances in terms of ARL, but the univariate approach signalled the first alarm with a longer delay with respect to competitor 2. The simplest image-based approach (competitor 4), i.e., the one that entails the univariate monitoring of the average pixel intensities of IR video frames, is also the one characterized by lowest performances. As a matter of fact, this approach is suitable to detect only the most severe out-of-control events characterized by a very large plume formation in the last layers. All these last three competitors were outperformed by the one based on the K-chart methodology. This highlights the enhanced effectiveness in detecting unstable process conditions when a non-parametric control charting scheme that adapts to the natural spread of monitored descriptors is used.

6 Conclusions

The enhancement of process capability and stability in LPBF is fundamental to meet the challenging requirements imposed by the industry in highly regulated sectors like aerospace and healthcare. A rapidly growing literature has been devoted to the characterization and monitoring of in-situ measured signatures as proxies of the process quality ad stability. This study proposed an LPBF monitoring method that exploits the plume generated by the laser-material interaction as information driver to quickly identify defects and unstable states. The presented case study consists of an LPBF process on zinc powder, which included both stable and unstable melting conditions. Despite of the industrial interest for additive manufacturing of zinc and its alloys in the biomedical sector, the low melting and boiling points of this material impose various challenges in LPBF in terms of process quality and stability. A statistical learning technique was proposed to monitor some relevant descriptors of the plume measured via in-situ IR video imaging. We proposed the use of the SVM methodology, first to extract the ROI via a maximum-margin partition of the variable space, then to design a nonparametric control chart known as K-chart. The K-chart is needed to cope with the multimode nature of the statistical descriptors of the ROI caused by the natural dynamics of the process. The application of the proposed approach to the zinc specimen production via LPBF showed that the plume can be used as a signature of the

process. The comparison study showed that the proposed approach is more effective than other methods that exploit traditional multivariate or univariate control charting schemes. The flexible control region generated by the K-chart allows a faster detection of process instabilities since their early stage, which is of great importance to quickly abort the process or to implement, when possible, feed-back control strategies.

Future developments will be aimed at investigating the feasibility of the proposed approach with different experimental setups and image streams acquired at higher frame rate. Indeed, high-speed IR video imaging is expected to enhance the characterization of the variability of plume formation during the laser scan, at the expense of challenging computational constraints that need to be faced. The study of the effect of environmental conditions on the plume properties also deserves additional experimental research. Finally, the feasibility of the method to detect other kinds of defect deserves future investigations too and it will be the subject of future studies.

Nomenclature

α	Type I error
α_j	Lagrangian multipliers
β	Type II error
ξ_j	Slack variables
μ_{pq}	Central moments
ϑ	ROI orientation angle
$A_{ROI,i}$	Area of the ROI
D_i	Distance of the i-th connected components from the scanned region
AM	Additive Manufacturing
ARL	Average run length
C	Penalty coefficients
f_s	Sampling frequency
g_i	Label of i-th connected component

h_d	Hatch distance
IC	In-control
$I(x, y)$	Pixel intensity
I_{ROI}	Average intensity of the ROI
IR	Infrared
K	Number of frames included into the training phase
$K(x)$	Kernel function
$kd(x)$	Kernel distance
$L(x)$	Lagrangian function
LHZ	Laser heated zone
LPBF	Laser powder bed fusion
$M \times N$	Size of IR images
M_{ROI}, N_{ROI}	Number of ROI pixels along the x and y directions
$\boldsymbol{o}$	Centre of the control region
OOC	Out-of-control
P	Laser power
R	Radius of the control region
RBF	Gaussian radial basis function
ROI	Region of interest
S	Kernel bandwidth
SVDD	Support Vector Data Description
SVM	Support Vector Machine
t	Layer thickness
T^2	Hotelling's statistic
$\boldsymbol{U}_j$	j-th IR video frame
v	Scan speed
$\boldsymbol{x}_j$	Monitored variable

References

[1] Gibson, I., Rosen, D. W., Stucker, B. (2010). Additive manufacturing technologies. New York: Springer.

[2] Grasso M., Colosimo B.M., (2017). Process Defects and In-situ Monitoring Methods in Metal Powder Bed Fusion: a Review, Measurement Science and Technology, 28(4), 1-25

[3] Everton, S. K., Hirsch, M., Stravroulakis, P., Leach, R. K., & Clare, A. T. (2016). Review of in-situ process monitoring and in-situ metrology for metal additive manufacturing. Materials & Design, 95, 431-445.

[4] Horn, T. J., Harrysson, O. L. (2012). Overview of current additive manufacturing technologies and selected applications. Science progress, 95(3), 255-282.

[5] Mellor, S., Hao, L., Zhang, D. (2014). Additive manufacturing: A framework for implementation. International Journal of Production Economics, 149, 194-201.

[6] Olakanmi, E. O., Cochrane, R. F., Dalgarno, K. W. (2015). A review on selective laser sintering/melting (SLS/SLM) of aluminium alloy powders: Processing, microstructure, and properties. Progress in Materials Science, 74, 401-477

[7] Frazier, W. E. (2014). Metal additive manufacturing: A review. Journal of Materials Engineering and Performance, 23(6), 1917-1928.

[8] Tapia, G., Elwany, A. (2014). A Review on Process Monitoring and Control in Metal-Based Additive Manufacturing. Journal of Manufacturing Science and Engineering, 136(6), 060801.

[9] Mani, M., Lane, B., Donmez, A., Feng, S., Moylan, S., & Fesperman, R. (2015). Measurement Science Needs for Real-time Control of Additive Manufacturing Powder Bed Fusion Processes, NISTIR 8036, http://dx.doi.org/10.6028/NIST.IR.8036

[10] Ponche, R., Kerbrat, O., Mognol, P., & Hascoet, J. Y. (2014). A novel methodology of design for Additive Manufacturing applied to Additive Laser Manufacturing process. Robotics and Computer-Integrated Manufacturing, 30(4), 389-398.

[11] García-Díaz, A., Panadeiro, V., Lodeiro, B., Rodríguez-Araújo, J., Stavridis, J., Papacharalampopoulos, A., & Stavropoulos, P. (2018). OpenLMD, an open source middleware and toolkit for laser-based additive manufacturing of large metal parts. Robotics and Computer-Integrated Manufacturing, 53, 153-161.

[12] Sing, S. L., Wiria, F. E., & Yeong, W. Y. (2018). Selective laser melting of lattice structures: A statistical approach to manufacturability and mechanical behavior. Robotics and Computer-Integrated Manufacturing, 49, 170-180.

[13] Ding, Y., Dwivedi, R., & Kovacevic, R. (2017). Process planning for 8-axis robotized laser-based direct metal deposition system: a case on building revolved part. Robotics and Computer-Integrated Manufacturing, 44, 67-76.

[14] Repossini G., Laguzza V., Grasso M., Colosimo B.M., (2018), On the use of spatter signature for in-situ monitoring of Laser Powder Bed Fusion, Additive Manufacturing, 16, 35-48. https://doi.org/10.1016 /j.addma.2017.05.004.

[15] Grasso, M., Demir, A. G., Previtali, B., & Colosimo, B. M. (2018). In situ monitoring of selective laser melting of zinc powder via infrared imaging of the process plume. Robotics and Computer-Integrated Manufacturing, 49, 229-239.

[16] Liu, Y., Yang, Y., Mai, S., Wang, D., & Song, C. (2015). Investigation into spatter behavior during selective laser melting of AISI 316L stainless steel powder. Materials & Design, 87, 797-806.

[17] Khairallah, S. A., Anderson, A. T., Rubenchik, A., & King, W. E. (2016). Laser powder-bed fusion additive manufacturing: Physics of complex melt flow and formation mechanisms of pores, spatter, and denudation zones. Acta Materialia, 108, 36-45.

[18] Andani, M. T., Dehghani, R., Karamooz-Ravari, M. R., Mirzaeifar, R., & Ni, J. (2017). Spatter formation in selective laser melting process using multi-laser technology. Materials & Design, 131, 460-469.

[19] Andani, M. T., Dehghani, R., Karamooz-Ravari, M. R., Mirzaeifar, R., & Ni, J. (2017). A Study on the Effect of Energy Input on Spatter Particles Creation during Selective Laser Melting Process. Additive Manufacturing.

[20] Ly, S., Rubenchik, A. M., Khairallah, S. A., Guss, G., & Matthews, M. J. (2017). Metal vapor micro-jet controls material redistribution in laser powder bed fusion additive manufacturing. Scientific reports, 7(1), 4085.

[21] King, W.E., Barth, H.D., Castillo, V.M., Gallegos, G.F., Gibbs, J.W., Hahn, D.E., Kamath, C., Rubenchik, A.M., (2014). Observation of keyhole-mode laser melting in laser powder-bed fusion additive manufacturing. J. Mater. Process. Technol., 214(12), 2915–2925

[22] Ye, D., Fuh, J. Y. H., Zhang, Y., Hong, G. S., & Zhu, K. (2018). In situ monitoring of selective laser melting using plume and spatter signatures by deep belief networks. In press in ISA Transactions.

[23] Wen, Q., & Gao, X. D. (2012). Classification of Plume Image and Analysis of Welding Stability during High Power Disc Laser Welding. In Applied Mechanics and Materials, 201, 1139-1142

[24] Gao, X. D., Qian, W. E. N., Katayama, S. (2013). Analysis of high-power disk laser welding stability based on classification of plume and spatter characteristics. Transactions of Nonferrous Metals Society of China, 23(12), 3748-3757.

[25] Chun-Ming Wang, Xuan-Xuan Meng, Wei Huang, Xi-Yuan Hu, Ai-Qin Duan, (2011). Role of side assisting gas on plasma and energy transmission during CO2 laser welding , Journal of Materials Processing Technology, 211, 668–674

[26] Zhao, C., Yao, Y., Gao, F., Wang, F. (2010). Statistical analysis and online monitoring for multimode processes with between-mode transitions. Chemical Engineering Science, 65(22), 5961-5975.

[27] Qin, S. J. (2012). Survey on data-driven industrial process monitoring and diagnosis. Annual Reviews in Control, 36(2), 220-234.

[28] Ge, Z., Song, Z., Gao, F. (2013). Review of recent research on data-based process monitoring. Industrial & Engineering Chemistry Research, 52(10), 3543-3562.

[29] Sun R., Tsung F., (2003). A Kernel-Distance-Based Multivariate Control Chart Using Support Vector Methods, International Journal of Production Research, 41(13), 2975-2989

[30] Camci F., Chinnam R. B., Ellis R. D. (2008). Robust Kernel Distance Multivariate Control Chart Using Support Vector Principles, International Journal of Production Research, 46(18), 5075-5095

[31] Sukchotrat T., Kim S. B., Tsung F. (2009). One-Class Classification-based Control Charts for Multivariate Process Monitoring, IIE Transactions, 42(2), 107-120

[32] Ge Z., Gao F., Song Z. (2011). Batch Process Monitoring Based on Support Vector Data Description Method, Journal of Process Control, 21, 949-959

[33] Gani W., Taleb H., Limam M. (2011). An Assessment of the Kernel-Distance-Based Multivariate Control Chart Through an Industrial Application, Quality and Reliability Engineering International, 27, 391-401

[34] Ning X., Tsung F., (2013). Improved Design of Kernel Distance-Based Charts Using Support Vector Methods, IIE Transactions, 45(4), 464-476

[35] Grasso M., Colosimo B.M., Semeraro Q., Pacella M. (2015). A Comparison Study of Distribution-Free Multivariate SPC Methods for Multimode Data, Quality & Reliability Engineering International, 31(1), 75 – 96

[36] Tax D.M.J., Duin R.P.W. (2004). Support Vector Data Description, Machine Learning, 54, 45-66

[37] Tax D. M. J. (2001). One-Class Classification; Concept-Learning In The Absence Of Counter-Examples, Ph.D. thesis, Delft University of Technology

[38] Kawahito, Y., Kinoshita, K., Matsumoto, N., Katayama, S. (2009). Visualization of refraction and attenuation of near-infrared laser beam due to laser-induced plume. Journal of laser applications, 21(2), 96-101.

[39] Bidare, P., Bitharas, I., Ward, R. M., Attallah, M. M., & Moore, A. J. (2018). Fluid and particle dynamics in laser powder bed fusion. *Acta Materialia*, *142*, 107-120.

[40] Zheng, H., Li, H., Lang, L., Gong, S., & Ge, Y. (2018). Effects of scan speed on vapor plume behavior and spatter generation in laser powder bed fusion additive manufacturing. *Journal of Manufacturing Processes*, *36*, 60-67.

[41] Mumtaz, K. A., & Hopkinson, N. (2010). Selective laser melting of thin wall parts using pulse shaping. *Journal of Materials Processing Technology*, *210*(2), 279-287.

[42] Zhang, J., Chen, G. Y., Zhou, Y., Li, S. C., Deng, H. (2013). Observation of spatter formation mechanisms in high-power fiber laser welding of thick plate, Applied Surface Science, 280, 868-875

[43] Hastie, T., Tibshirani, R., Friedman, J. (2009). The elements of statistical learning, 2(1). Springer, New York

[44] Li, C. H., Lin, C. T., Kuo, B. C., & Chu, H. S. (2010). An automatic method for selecting the parameter of the RBF kernel function to support vector machines. In Geoscience and Remote Sensing Symposium (IGARSS), 2010 IEEE International (pp. 836-839). IEEE.

[45] L. Xu, J. Neufeld, B. Larson, and D. Schuurmans (2004). Maximum margin clustering. In Advances in Neural Information Processing Systems.

[46] Kaplan, A. F. H., Mizutani, M., Katayama, S., Matsunawa, A., (2002). Unbounded keyhole collapse and bubble formation during pulsed laser interaction with liquid zinc. J. Phys. D. Appl. Phys. 35. 1218–1228

[47] Lane S., Martin E. B., Kooijmans R., Morris A. J. (2001). Performance monitoring of a multiproduct semi-batch process, Journal of Process Control, 11(1), 1-11

[48] Hwang D. H., Han C. (1999). Real-time monitoring for a process with multiple operating modes, Control Engineering Practice, 7(7), 891–902

[49] Choi S. W., Park J. H., Lee I. B. (2004). Process monitoring using a Gaussian mixture model via principal component analysis and discriminant analysis, Computers and Chemical Engineering, 28, 1377-1387

[50] Grasso, M., Colosimo, B. M., & Tsung, F. (2017). A phase I multi-modelling approach for profile monitoring of signal data. International Journal of Production Research, 55(15), 4354-4377.

[51] Y. F. Zheng, X. N. Gu, and F. Witte, (2014). Biodegradable metals, Mater. Sci. Eng. R Reports, 77, 1–34

[52] Montani M., Demir, A.G., Mostaed, E., (2016). Processability of pure Zn and pure Fe by SLM for biodegradable metallic implant manufacturing, Rapid Prototyping Journal, Accepted article, 10.1108/RPJ-08-2015-0100

[53] Montgomery, D. C. (2009). Statistical quality control (Vol. 7). New York: Wiley.

[54] Bowman, A. W., Azzalini A. (1997). Applied Smoothing Techniques for Data Analysis, Oxford University Press, New York